

# Spatio-temporal modeling of urban extreme rainfall events at high resolution

Chloe Serre-Combe<sup>1,\*</sup>, Nicolas Meyer<sup>1</sup>, Thomas Opitz<sup>2</sup>, and Gwladys Toulemonde<sup>1</sup>

<sup>1</sup>IMAG, Univ. Montpellier, CNRS, Inria LEMON team, Montpellier, France

<sup>2</sup>BioSP, Inrae, Avignon, France

\*Corresponding author: [chloe.serre-combe@umontpellier.fr](mailto:chloe.serre-combe@umontpellier.fr)

## Abstract

Modeling precipitation and its accumulation over time and space is essential for flood risk assessment. We here analyze rainfall data collected over several years through a micro-scale precipitation sensor network in Montpellier, France, by the OMSEV observatory. A novel spatio-temporal stochastic model is proposed for high-resolution urban rainfall and combines realistic marginal behavior and flexible extremal dependence structure. Rainfall intensities are described by the Extended Generalized Pareto Distribution (EGPD), capturing both moderate and extreme events without threshold selection. Based on spatial extreme-value theory, dependence during extreme episodes is modeled by an  $r$ -Pareto process with a non-separable variogram including episode-specific advection, allowing the displacement of rainfall cells to be represented explicitly. Parameters are estimated by a composite likelihood based on joint exceedances, and empirical advection velocities are derived from radar reanalysis. The model accurately reproduces the spatio-temporal structure of extreme rainfall observed in the Montpellier OMSEV network and enables realistic stochastic scenario generation for flood risk assessment.

**Keywords:** Extreme value theory, EGPD, high spatio-temporal resolution,  $r$ -Pareto process, advection

## 1. Introduction

Rainfall modeling is essential in evaluating flood risks and analyzing the impact of urbanization, particularly in areas such as the Cévennes mountain range and the coastal agglomeration of the city of Montpellier in the south of France. The Cévennes massif is known for its specific climatological features, experiencing some of the most extreme rainfall in France, especially during the autumn season. The topography of these mountains acts as a barrier to relatively

warm and humid air masses from the Mediterranean sea making landfall, which causes atmospheric instability and orographic uplift. These conditions lead to intense rainfall events that can sometimes exceed 500 mm within a 24-hour period, as evidenced by historical occurrences such as the significant floods in Anduze in 2002 with 680 mm of rain in 24 hours (Fouchier et al. 2004), which is more than the annual average rainfall amount in Paris (see Hempelmann et al. 2021). Such events are characterised by a large amount of rainfall occurring over short durations and are often highly localized, possibly leading to severe flooding, especially flash floods.

The city of Montpellier also faces such extreme rainfall events, for instance in September 2014 with a total of 260 mm of rain falling in only four hours (see Brunet et al. 2018), or more recently with a total of 100 mm in seven hours recorded on December 22, 2025 by the Meteo France station of Montpellier airport ([meteo.data.gouv.fr](https://meteo.data.gouv.fr)). The city's proximity to the Cévennes mountains exacerbates these flooding risks, underscoring the necessity for precise rainfall modeling and simulations for effective flood risk assessment and urban planning. The highly localized nature of these weather events emphasizes the importance of understanding rainfall behavior at a high spatio-temporal resolution.

In this context, a rain-gauge network has been deployed in Montpellier by the OMSEV observatory, detailed in Section 2.1. This network provides high-resolution rainfall measurements that aim to help in the analysis of urban flood processes and their impacts within a hydrological model developed at Inria Montpellier. However, these data present several challenges, including a relatively short observation period, a high proportion of missing values, and the sparsity of non-zero rainfall observations, which complicate statistical modeling and inference. Addressing these challenges constitutes a central objective of this paper in order to develop a stochastic precipitation generator that can be used to simulate realistic rainfall fields at high spatio-temporal resolution, while accounting for advection effects driving the spatial displacement of rainfall events.

This paper is organized as follows. Section 2 presents the data used in this study, together with related work and the methodological background for the proposed stochastic precipitation generator. Section 3 introduces the complete statistical model for extreme rainfall, combining an EGPD for the marginal distributions with the  $r$ -Pareto process to capture spatio-temporal dependence. Estimation procedures for the model parameters are detailed in Section 4, including the incorporation of advection effects. Section 5 applies the proposed framework to the OMSEV rainfall data to estimate the model parameters. Section 6 presents the simulations of extreme rainfall fields based on the fitted model over the OMSEV network, evaluates its performance in reproducing the spatio-temporal structure of extreme rainfall events. Finally, Section 7 concludes the paper with a discussion of the results and potential future research directions.

## 2. Data and methodological background

In this section, we present the datasets used in this work and provide the related works and methodological background for the proposed spatio-temporal stochastic precipitation generator.

### 2.1 Case study and datasets

Our study focuses on the OMSEV<sup>1</sup> rain gauge network, located within the Verdanson river catchment, a tributary of the Lez river (see [Figure 1](#)), flowing into the Mediterranean Sea around 10 km South of Montpellier. This network consists of 20 tipping-bucket rain gauges installed by the urban observatory of HydroSciences Montpellier ([Finaud-Guyot et al. 2023](#)). Although tipping-bucket rain gauges provide high-resolution measurements, they can lead to an underestimation of rainfall intensities. A proper calibration was therefore done by hydrologists of each rain gauge in order to obtain the most reliable estimates of rainfall intensity ([Robin 2021](#)). We exclude three rain gauges installed only recently that do not yet provide sufficiently long data series (CINES, Brives and Hydropolis, see [Figure 1b](#)). The dataset covers the period from September 2019 to January 2025 and provides rainfall measurements at high temporal resolution, recorded every minute leading to discretized low values. In order to reduce measurement errors, to decrease data volume and to avoid overly discretized values, the data are aggregated in 5-minute intervals which preserve a high temporal resolution. It allows to reduce the number of missing values that are considered as 0 over these intervals when there is at least one non-missing value, which are more frequent at the original minute resolution. At this temporal resolution, approximately 23% of data are missing, due to activation dates of each rain gauges and measurement errors and are not imputed in the present work. With this fine resolution, a kind of discretization is still present for very low values, and the proportion of non-zero values is very low, representing only 1.2% of the data. Spatial granularity is also very fine with inter-site distance ranging from 77 to 1531 meters (without removed gauges). Data from urban microscale rain gauge networks like this are very scarce (e.g. [Casas et al. 2010](#) for Barcelona, Spain) but can provide important insights rainfall patterns known to be highly variable and complex even at very small spatio-temporal scales.

---

<sup>1</sup>Observatoire Montpelliérain et au Sud de l'Eau dans la Ville

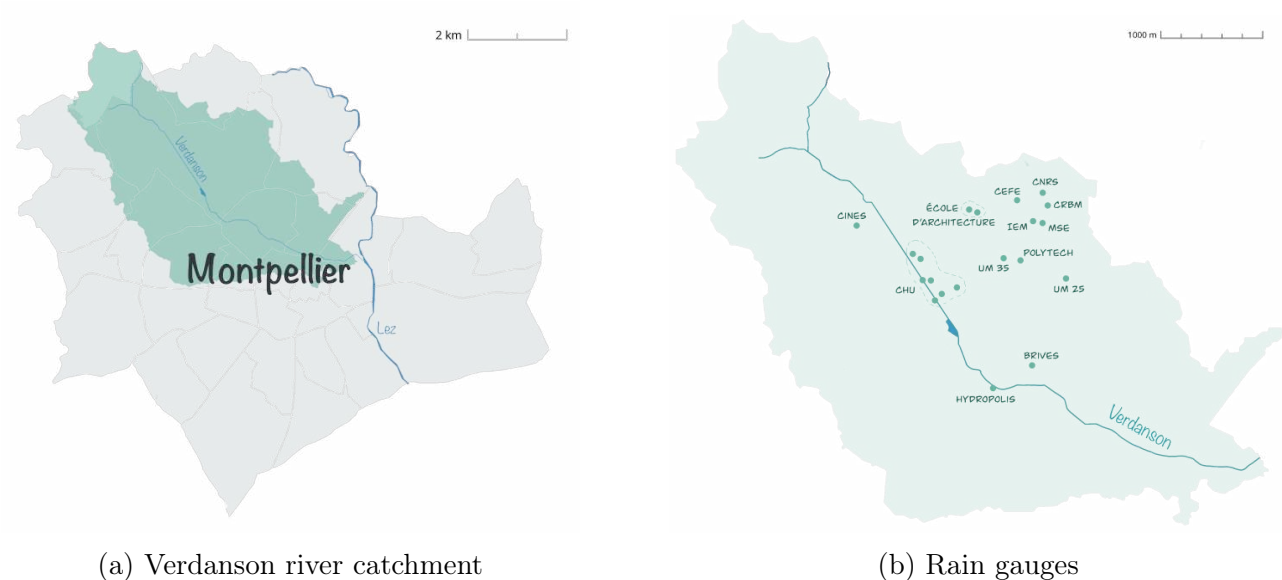


Figure 1: Location of the 20 rain gauges of the OMSEV network over the Verdanson river catchment in Montpellier

The rain gauges of the OMSEV network are irregularly distributed. A more regular spatial grid would be desirable for rainfall field modeling. In addition, the relatively short temporal coverage of the OMSEV dataset may not fully capture important features and the variability of extreme rainfall events. To address these limitations, we enrich these data with the French COMEPHORE<sup>2</sup> mosaic from Météo France (see Tabary et al. 2012). COMEPHORE is a reanalysis product combining radar and rain gauge observations over France, provided on a regular grid with a spatial resolution of 1 km<sup>2</sup> per pixel and an hourly temporal resolution. The dataset spans from 1997 to 2024. We restrict the analysis to after 2008 due to a change in the reanalysis model in 2007 inducing possible distributional changes. We extract the data over the same area as the OMSEV network, corresponding to 111 pixels within a 5 km radius of the network centroid, which is sufficient to represent the local spatial variability. Only five of these pixels contain OMSEV rain gauges or seven pixels when considering also removed gauges (see Figure 2).

<sup>2</sup>COmbinaison en vue de la Meilleure Estimation de la Précipitation HOraiRE. The dataset is available on AERIS platform (<https://radarsmf.aeris-data.fr/>)

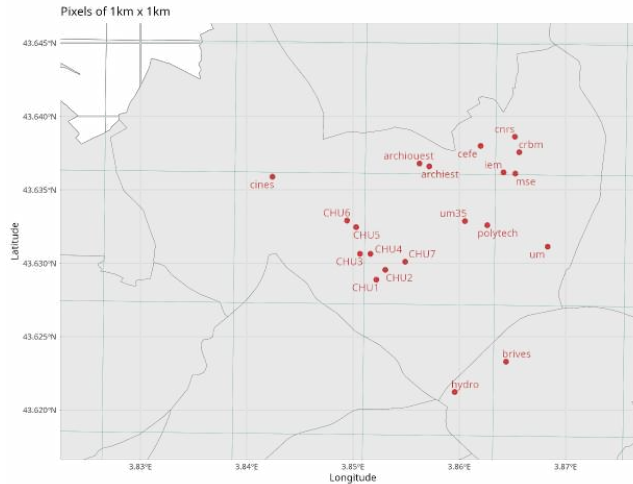


Figure 2: Location of the 20 rain gauges of the OMSEV network (red dots) over the COMEPHORE reanalysis (blue grid).

## 2.2 State of the art and proposed methodological framework

We aim to model and simulate realistic high-resolution spatio-temporal rainfall fields over the Montpellier area and put focus on extreme precipitation events relevant for flood risk analysis. Physics-based global and regional climate simulation models provide valuable information at relatively large scales, especially for continental to global analyses, with resolutions around 10 to 100 km. However, their spatial and temporal resolutions remain too coarse to accurately represent short-duration, high-intensity, and highly localized rainfall events, despite the recent development of convection-permitting simulations models with kilometer resolution (Lucas-Picher et al. 2021). Moreover, their high computational cost prevents the generation of large ensembles required for probabilistic risk assessment.

In this context, stochastic weather generators (SWGs) constitute a complementary and computationally efficient alternative (Wilks and Wilby 1999). Within this class of models, stochastic precipitation generators (SPGs) specifically focus on rainfall and aim to reproduce its main statistical characteristics, including occurrence, intensity, duration, and spatial structure. Designing SPGs is challenging due to the highly non Gaussian distribution of rainfall, typically with heavy tails and a large proportion of zeros, and the need to provide simulations that are explicit and coherent in space and time, for using them as inputs of numerical impact models. Early developments and methodological overviews highlight the diversity of SPG frameworks and their ability to capture rainfall variability across a range of spatial and temporal scales (Allard et al. 2015). In particular, geostatistical simulation approaches have been shown to effectively reproduce spatial rainfall structures (Benoit and Mariethoz 2017). Several studies have shown that SPGs can be developed at sub-kilometer and sub-hourly resolutions, and have highlighted the importance of advection or wind consideration for reproducing fine-scale

space–time rainfall dynamics (Leblois and Creutin 2013, Schleiss et al. 2014, Huser and Davison 2014). More recently, Benoit et al. 2018 proposed a meta-Gaussian framework to generate realistic high-resolution rainfall fields, considering advection effects.

Rainfall intensities exhibit different regimes, ranging from dry periods to moderate and extreme precipitation. Since extreme rainfall plays a key role in flooding, extreme value theory (EVT) provides a natural framework for its statistical modeling. Classical EVT approaches include block maxima models based on the Generalized Extreme Value (GEV) distribution and Peaks-Over-Threshold (POT) models based on the Generalized Pareto Distribution (GPD). In practice, POT approaches are often preferred as they retain more extreme observations and offer greater flexibility, especially for modeling temporal patterns. However, their performance strongly depends on the choice of a threshold, which is known to be challenging and to significantly affect inference results, as highlighted in reviews by Coles et al. 2001 and Scarrott and MacDonald 2012. To avoid explicit threshold selection and to model the entire range of rainfall intensities, mixture models have been proposed, combining a distribution for moderate rainfall with a GPD tail (Carreau and Bengio 2009). These approaches still require a transition threshold and induce a dependence between bulk and tail behavior (Naveau et al. 2016). To overcome these limitations, the class of Extended Generalized Pareto Distributions (EGPDs) (Papastathopoulos and Tawn 2013, Naveau et al. 2016) can be used. It provides a unified model for strictly positive variables without threshold selection. EGPDs allow a flexible representation of both moderate and extreme rainfall and have already proven their efficiency in precipitation modeling applications (Haruna et al. 2023, Carrer and Gaetan 2022).

While marginal modeling is essential, realistic rainfall simulations also require an adequate representation of spatio-temporal dependence. In the context of extremes, this dependence is commonly described using asymptotic models such as max-stable and Pareto processes (Davison et al. 2012, Ferreira and De Haan 2014), which provide a natural framework for spatio-temporal extreme events and allow extrapolation beyond observed extremes. However, max-stable models are computationally demanding and difficult to handle in high-dimensional environmental settings (Davison et al. 2013). To overcome these limitations, we rely on the Brown-Resnick  $r$ -Pareto process (De Fondeville and Davison 2018, Dombry et al. 2024), which arises as a limiting model for threshold exceedances of stochastic processes. This model preserves the dependence structure of the max-stable Brown-Resnick process while offering greater flexibility and improved computational efficiency compared with max-stable models, making it particularly suitable for spatio-temporal modeling of extreme rainfall.

In the present work, we propose a novel framework for the simulation of high-resolution extreme rainfall fields that models moderate and extreme marginals with a spatio-temporal extremal dependence. The proposed approach specifically targets extreme rainfall episodes relying on the Extended Generalized Pareto Distribution (EGPD) of Naveau et al. 2016 for the marginal modeling of rainfall intensities. In contrast to recent high-resolution stochastic precipitation modeling studies, our approach focuses on reproducing the spatio-temporal dependence of extremes through the estimation of variogram parameters using a composite likelihood based

on joint exceedances from identified extreme episodes. A key contribution of this work is the explicit incorporation of event-specific advection effects into the dependence structure via a non-separable spatio-temporal variogram. While similar ideas have been explored for max-stable processes using wind information at coarser resolutions and over larger spatial domains (Huser and Davison 2014), our approach, developed on  $r$ -Pareto processes, focuses on threshold exceedances and high-resolution urban rainfall data. The episode-specific advection term explicitly accounts for the displacement of rainstorms over time. This framework enables the simulation of realistic, high-resolution, moving extreme precipitation fields over a given spatial domain. We apply the proposed methodology to rainfall simulation on a grid covering the OMSEV network in the Montpellier area.

### 3. Spatio-temporal modeling for extreme precipitation

Let  $\mathbf{X} = \{X_{\mathbf{s},t} \mid (\mathbf{s}, t) \in \mathcal{S} \times \mathcal{T}\}$  be a nonnegative spatio-temporal random field representing the rainfall intensity for all locations  $\mathbf{s}$  in a spatial domain  $\mathcal{S} \subset \mathbb{R}^2$  and all times  $t$  in a temporal domain  $\mathcal{T} \subset \mathbb{R}_+$ . Let  $\Lambda_{\mathcal{S}} \subset \mathbb{R}^2$  and  $\Lambda_{\mathcal{T}} \subset \mathbb{R}$  be the sets of spatial and temporal lags, respectively. In the following, we present the proposed model the construction of the stochastic process  $\mathbf{X}$  for extreme rainfall, which combines a flexible marginal distribution using EGPD and a spatio-temporal dependence structure based on the  $r$ -Pareto process.

#### 3.1 Marginal rainfall distributions

Rainfall at high temporal resolution is characterized by a large proportion of zero values, corresponding to dry periods. To account for this structure, rainfall at each site is modeled using a mixed distribution with a point mass at zero and a distribution for positive values.

##### 3.1.1 Modeling positive rainfall intensities

Let  $X_{\mathbf{s}}$  be the rainfall intensity at a fixed location  $\mathbf{s}$ . To model the whole marginal distribution of positive rainfall intensities, we use the Extended Generalized Pareto Distribution (EGPD). The EGPD is constructed as an extension of the classical Generalized Pareto Distribution (GPD), which corresponds to the limit distribution of threshold exceedances. For a sufficiently large threshold  $u$ , the distribution of the exceedances can be approximated by a GPD with shape parameter  $\xi$  and scale parameter  $\sigma_u$ :

$$\mathbb{P}(X_{\mathbf{s}} - u > y \mid X_{\mathbf{s}} > u) \approx \overline{H}_{\xi}\left(\frac{y}{\sigma_u}\right) = \begin{cases} \left(1 + \xi \frac{y}{\sigma_u}\right)_+^{-1/\xi}, & \text{if } \xi \neq 0, \\ \exp\left(-\frac{y}{\sigma_u}\right), & \text{if } \xi = 0, \end{cases} \quad y > 0,$$

where  $(a)_+ = \max(a, 0)$ . The EGPD is then defined by considering a polynomial transformation  $P(x) = x^{\kappa}$ , with  $\kappa > 0$  of the GPD. This is the simplest and most efficient choice among other transformations proposed by Naveau et al. 2016. The EGPD preserves the GP behavior

of the upper tail while extending the model to moderate rainfall values through a smooth transformation of the GPD distribution. The corresponding shape is driven by the parameter  $\kappa$ . We define  $F_{\text{EGPD}}$  as the EGPD cumulative distribution function with parameters  $(\xi, \sigma, \kappa)$ , independent of the threshold  $u$ . Then

$$X_{\mathbf{s}} \mid X_{\mathbf{s}} > 0 \sim F_{\text{EGPD}}(\xi, \sigma, \kappa).$$

### 3.1.2 Overall marginal model

Let  $p_0$  be the marginal probability of zero rainfall for each location  $\mathbf{s}$ . Given that  $X_{\mathbf{s},t} > 0$ , positive rainfall amounts are assumed to follow an EGPD. For a fine spatio-temporal resolution it is reasonable to consider constant parameters  $(\xi, \sigma, \kappa)$  over the spatial domain and over time. Then the EGPD distribution is the same for all  $\mathbf{s} \in \mathcal{S}$  and  $t \in \mathcal{T}$ . The resulting marginal distribution for  $x \in \mathbb{R}$  function is given by

$$F(x) = \begin{cases} p_0, & x = 0, \\ p_0 + (1 - p_0) F_{\text{EGPD}}(x), & x > 0. \end{cases}$$

This expression allows the dry-period frequency and the distribution of positive rainfall intensities to be modeled separately, while keeping a coherent marginal model.

## 3.2 Spatio-temporal extremal dependence

To model the spatio-temporal dependence of extreme rainfall, we consider the  $r$ -Pareto process introduced by [De Fondeville and Davison 2018](#). This process provides a natural framework for modeling the dependence structure of exceedances above high thresholds.

We consider a regularly varying spatio-temporal process  $\mathbf{X}$  in the maximum domain of attraction of a max-stable process, and a nonnegative and 1-homogeneous risk function  $r$ , that is, a function satisfying  $r(a\mathbf{X}) = ar(\mathbf{X})$  for any  $a > 0$ . As shown by [Dombry et al. 2024](#), the  $r$ -exceedances of  $\mathbf{X}$  converge in distribution to an  $r$ -Pareto process  $\mathbf{Y} = \{Y_{\mathbf{s},t} \mid (\mathbf{s}, t) \in \mathcal{S} \times \mathcal{T}\}$ :

$$u^{-1}X_{\mathbf{s},t} \mid r(\mathbf{X}) > u \xrightarrow{d} Y_{\mathbf{s},t}, \quad u \rightarrow \infty.$$

To model the dependence structure of  $\mathbf{Y}$ , we assume a Brown-Resnick representation induced by an underlying Gaussian process  $\mathbf{W} = \{W_{\mathbf{s},t}, (\mathbf{s}, t) \in \mathcal{S} \times \mathcal{T}\}$  with stationary increments. The dependence structure of the process is then characterized through its spatio-temporal variogram  $\gamma$  of the underlying Gaussian process defined for any  $(\mathbf{h}, \tau) \in \Lambda_{\mathcal{S}} \times \Lambda_{\mathcal{T}}$  as

$$\gamma(\mathbf{h}, \tau) = \frac{1}{2} \mathbb{V}(W_{\mathbf{s}+\mathbf{h}, t+\tau} - W_{\mathbf{s},t}).$$

In this paper we consider the risk function  $r(\mathbf{X}) = X_{\mathbf{s}_0, t_0}$  where  $(\mathbf{s}_0, t_0) \in \mathcal{S} \times \mathcal{T}$  corresponds to a fixed reference spatio-temporal location. The corresponding  $r$ -Pareto process can be represented

as

$$Y_{\mathbf{s},t} = R \exp(W_{\mathbf{s},t} - W_{\mathbf{s}_0,t_0} - \gamma(\mathbf{s} - \mathbf{s}_0, t - t_0)),$$

where  $R$  follows a univariate Pareto distribution, that is,  $\mathbb{P}(R > v) = v^{-1}$  for  $v \geq 1$ . This approach is relevant since it links the variogram of the underlying Gaussian process to the dependence structure of the  $r$ -Pareto process  $\mathbf{Y}$ . Thus it allows to capture the main features of the extremal dependence structure of the process  $\mathbf{X}$  with respect to the conditional exceedance at  $(\mathbf{s}_0, t_0) \in \mathcal{S} \times \mathcal{T}$  given by the risk function.

In EVT, extremal dependence can be summarized through the spatio-temporal extremogram which corresponds to the probability that an exceedance at one location and time occurs given an exceedance at another location and time. Following [Coles et al. 1999](#), the extremal dependence coefficient is defined for spatial lag  $\mathbf{h} \in \Lambda_{\mathcal{S}}$  and temporal lag  $\tau \in \Lambda_{\mathcal{T}}$  as

$$\chi(\mathbf{h}, \tau) = \lim_{q \rightarrow 1} \mathbb{P}(X_{\mathbf{s},t}^* > q \mid X_{\mathbf{s}+\mathbf{h},t+\tau}^* > q),$$

where  $X_{\mathbf{s},t}^*$  denotes the uniform marginal transformation of  $X_{\mathbf{s},t}$ . The coefficient  $\chi(\mathbf{h}, \tau)$  ranges from 0 (asymptotic independence) to 1 (perfect extremal dependence). For the chosen  $r$ -Pareto process, the extremal dependence of  $\mathbf{X}$  can be summarized through the  $r$ -extremogram

$$\chi_r(\mathbf{h}, \tau) = \lim_{u \rightarrow \infty} \mathbb{P}(X_{\mathbf{s}_0+\mathbf{h},t_0+\tau} > u \mid X_{\mathbf{s}_0,t_0} > u) = \lim_{u \rightarrow \infty} \mathbb{P}(X_{\mathbf{s}_0+\mathbf{h},t_0+\tau} > u),$$

which describes the extremal dependence structure of  $\mathbf{X}$  with respect to the conditional exceedance. This implies that  $\mathbb{P}(X_{\mathbf{s}_0,t_0} > u) = 1$  for large  $u$ . Under the Brown-Resnick model representation, this coefficient depends directly on the variogram and can be expressed as

$$\chi_r(\mathbf{h}, \tau) = 2 \left( 1 - \Phi \left( \sqrt{\frac{1}{2} \gamma(\mathbf{h}, \tau)} \right) \right), \quad (1)$$

where  $\Phi$  denotes the standard normal distribution function (see [Buhl et al. 2019](#)) and  $(\mathbf{h}, \tau) = (\mathbf{s} - \mathbf{s}_0, t - t_0) \in \Lambda_{\mathcal{S}} \times \Lambda_{\mathcal{T}}$  represents the space-time lag with respect to the reference location. This formulation entails that small values of  $\gamma(\mathbf{h}, \tau)$  correspond to strong extremal dependence, whereas large variogram values imply weak dependence.

### 3.3 Non-separable space-time variogram with advection

A common approach to model spatio-temporal dependence consists in considering the variogram as a sum of purely spatial and purely temporal components. In these so-called separable models, the spatio-temporal variogram is expressed as

$$\gamma(\mathbf{h}, \tau) = \gamma_{\mathcal{S}}(\mathbf{h}) + \gamma_{\mathcal{T}}(\tau), \quad \mathbf{h} \in \Lambda_{\mathcal{S}}, \tau \in \Lambda_{\mathcal{T}},$$

where  $\gamma_{\mathcal{S}}$  and  $\gamma_{\mathcal{T}}$  are purely spatial and purely temporal variograms, respectively.

Separable spatio-temporal variogram models provide a simple and reasonable description of

the overall dependence structure of rainfall data. However, they fail to capture the complex interactions between space and time, especially in the context of meteorological phenomena and in particular for extreme rainfall events. Extreme precipitation is often driven by dynamical mechanisms, such as advection that induce strong interactions between space and time. In meteorology, it corresponds to the horizontal transport of properties (heat, moisture) by the movement of air masses, such as wind and clouds. This phenomenon therefore influences the spatio-temporal behavior of precipitations, but cannot be adequately captured by a separable model and requires non-separable spatio-temporal structures.

To construct a non-separable variogram accounting for advection, we start from a spatio-temporal process with stationary increments, whose spatial and temporal variograms are, for spatial lag  $\mathbf{h} \in \Lambda_{\mathcal{S}}$  and temporal lag  $\tau \in \Lambda_{\mathcal{T}}$ ,

$$\gamma_{\mathcal{S}}(\mathbf{h}) = 2\beta_1 \|\mathbf{h}\|^{\alpha_1}, \quad \gamma_{\mathcal{T}}(\tau) = 2\beta_2 |\tau|^{\alpha_2},$$

with  $\beta_1, \beta_2 > 0$  and  $\alpha_1, \alpha_2 \in (0, 2]$ . Without advection, this leads to a separable spatio-temporal variogram.

Advection is incorporated through a deterministic space-time shift defined by a velocity vector  $\mathbf{V} \in \mathbb{R}^2$ , yielding the non-separable variogram

$$\gamma(\mathbf{h}, \tau; \Theta, \mathbf{V}) = 2(\beta_1 \|\mathbf{h} - \tau \mathbf{V}\|^{\alpha_1} + \beta_2 |\tau|^{\alpha_2}),$$

where  $\Theta = (\beta_1, \beta_2, \alpha_1, \alpha_2)$ . The corresponding  $r$ -extremogram follows from [Equation 1](#) and is denoted by  $\chi_r(\mathbf{h}, \tau; \Theta, \mathbf{V})$ .

### 3.4 Stochastic precipitation generator

The stochastic precipitation generator is constructed by combining the marginal model for rainfall amounts with the dependence model for extremes based on the  $r$ -Pareto process.

The  $r$ -Pareto process  $\mathbf{Y}$  describes the dependence structure of extreme events on a standardized Pareto scale and does not carry information on their real magnitude. To reintroduce the intensity level of extreme episodes, simulations are rescaled by a high threshold  $u$ , leading to the spatio-temporal process

$$\mathbf{Z} = \{Z_{\mathbf{s},t} = u Y_{\mathbf{s},t} \mid (\mathbf{s}, t) \in \mathcal{S} \times \mathcal{T}\}.$$

By construction,  $Z_{\mathbf{s},t}$  has Pareto tails with  $\mathbb{P}(Z_{\mathbf{s},t} > z) = \frac{u}{z}$ , for  $z > u$ .

To combine this dependence model with the rainfall marginal distributions, the simulated values on the Pareto scale are mapped to the unit interval using a standardisation function  $G$

following [Palacios-Rodríguez et al. 2020](#). The function  $G$  is defined as

$$G(x) = \begin{cases} 0, & x < 0, \\ p_0, & x = 0, \\ p_0 + \frac{(1-p_0)^2}{4}x, & 0 < x < \frac{2}{1-p_0}, \\ 1 - \frac{1}{x}, & x > \frac{2}{1-p_0}. \end{cases}$$

This transformation preserves the tail behavior of the  $r$ -Pareto model and puts a point mass at zero. Applying this transformation  $G$  to the process  $\mathbf{Z}$ , we obtain the simulated values on the uniform scale,

$$U_{\mathbf{s},t} = G(Z_{\mathbf{s},t}), \quad \mathbf{s} \in \mathcal{S}, t \in \mathcal{T}.$$

The simulated rainfall process are obtained by applying the inverse marginal distribution function,

$$X_{\mathbf{s},t} = F^{-1}(U_{\mathbf{s},t}), \quad \mathbf{s} \in \mathcal{S}, t \in \mathcal{T},$$

where

$$F^{-1}(x) = \begin{cases} 0, & x \leq p_0, \\ F_{\text{EGPD}}^{-1}\left(\frac{x-p_0}{1-p_0}; \xi, \sigma, \kappa\right), & x > p_0. \end{cases}$$

This approach allows the generation of spatio-temporal rainfall fields reproducing both the intensity and the dependence structure of extreme precipitation events.

## 4. Estimation of model parameters

In this section, we present the estimation procedures for the parameters of the proposed model, including the marginal parameters, the episode selection procedure and the estimation of the variogram parameters with advection effects using a composite likelihood based on joint exceedances.

### 4.1 Marginal parameter estimation

The marginal parameters  $(p_0, \xi, \sigma, \kappa)$  are estimated separately at each location  $\mathbf{s} \in \mathcal{S}$  and then averaged over all locations to obtain a single set of parameters for the entire spatial domain. The probability of zero rainfall  $p_0$  is estimated by the empirical proportion of zero values at location  $\mathbf{s}$  and the EGPD parameters  $(\xi, \sigma, \kappa)$  are estimated by maximum likelihood using only positive rainfall values.

### 4.2 Selection of extreme episodes

Let  $\delta > 0$  denote a fixed temporal duration for extreme episodes. For each conditioning exceedance occurring at location  $\mathbf{s}_0 \in \mathcal{S}$  and time  $t_0 \in \mathcal{T}$ , we define an extreme episode from

the process  $\mathbf{X}$  with a duration  $\delta$  and starting at time  $t_0$ :

$$\mathbf{E} = \{X_{\mathbf{s},t} \mid X_{\mathbf{s}_0,t_0} > u, \mathbf{s} \in \mathcal{S}, t \in [t_0, t_0 + \delta[ \}.$$

Extreme episodes are selected following a procedure described by [Palacios-Rodríguez et al. 2020](#), which ensures a weak dependence between episodes. First we identify all possible conditioning exceedances above a high threshold  $u$ , *i.e.* all spatio-temporal locations  $(\mathbf{s}_0, t_0) \in \mathcal{S} \times \mathcal{T}$  such that  $X_{\mathbf{s}_0,t_0} > u$ . Then, these conditioning exceedances are ordered by time and processed in chronological order. An episode with conditioning location  $(\mathbf{s}_0, t_0) \in \mathcal{S} \times \mathcal{T}$  is retained if for every already selected episode with conditioning location  $(\mathbf{s}'_0, t'_0) \in \mathcal{S} \times \mathcal{T}$  we have

$$\|\mathbf{s}'_0 - \mathbf{s}_0\| \geq d_{\min} \quad \text{or} \quad |t'_0 - t_0| \geq \delta,$$

where  $d_{\min} > 0$  is a minimum spatial separation and the temporal separation is given by the episode duration  $\delta$ . In other words, all potential episodes falling within the spatio-temporal neighborhood of an already selected episode are discarded from further consideration. The procedure stops when either a fixed maximum number of episodes is reached or no exceedance above  $u$  remains. The resulting set of selected episodes is denoted by  $\mathcal{E}$ .

### 4.3 Composite likelihood based on exceedances

For each episode  $\mathbf{E} \in \mathcal{E}$ , spatio-temporal neighbors are defined relatively to the conditioning point  $(\mathbf{s}_0, t_0) \in \mathcal{S} \times \mathcal{T}$ . The corresponding neighborhood, *i.e.* the set of all spatio-temporal locations at given lags from the conditioning point, is defined as

$$\mathcal{N}_{\mathbf{E}}(\mathbf{h}, \tau) = \{(\mathbf{s}, t) \in \mathcal{S} \times \mathcal{T} \mid \|\mathbf{s} - \mathbf{s}_0\| \in C_{\mathbf{h}}, |t - t_0| \in C_{\tau}\},$$

where  $C_{\mathbf{h}}$  and  $C_{\tau}$  denote predefined spatial and temporal lag classes. In practice, if a regular spatio-temporal grid is considered, these classes are defined as direct spatial and temporal lags sets. For each location  $(\mathbf{s}, t) \in \mathcal{N}_{\mathbf{E}}(\mathbf{h}, \tau)$ , we define the indicator variable of joint exceedances as

$$k_{\mathbf{E}}(\mathbf{s}, t) = \mathbb{1}_{\{X_{\mathbf{s},t} > u, X_{\mathbf{s}_0,t_0} > u\}} = \mathbb{1}_{\{X_{\mathbf{s},t} > u\}}$$

where the conditioning exceedance  $X_{\mathbf{s}_0,t_0} > u$  holds by construction. With the  $r$ -Pareto model,  $k_{\mathbf{E}}(\mathbf{s}, t)$  follows a Bernoulli distribution with success probability  $\chi_r(\mathbf{h}, \tau; \Theta, \mathbf{V}_{\mathbf{E}})$  with parameters  $\Theta = (\beta_1, \beta_2, \alpha_1, \alpha_2)$  and episode-specific velocity vectors  $\mathbf{V}_{\mathbf{E}}$ . The number of exceedances at lag  $(\mathbf{h}, \tau)$  during an episode is then given by

$$K_{\mathbf{E}}(\mathbf{h}, \tau) = \sum_{(\mathbf{s}, t) \in \mathcal{N}_{\mathbf{E}}(\mathbf{h}, \tau)} k_{\mathbf{E}}(\mathbf{s}, t).$$

After aggregating over all episodes, we obtain the total number of exceedances and a total number of trials for lag  $(\mathbf{h}, \tau)$  that are given by

$$K_{\text{tot}}(\mathbf{h}, \tau) = \sum_{\mathbf{E} \in \mathcal{E}} K_{\mathbf{E}}(\mathbf{h}, \tau),$$

These aggregated exceedance counts provide the basis for the composite likelihood used to estimate the variogram parameters. Under approximate independence between episodes and for large  $u$ , Bernoulli likelihood contributions are used to construct the composite likelihood. The resulting composite log-likelihood satisfies

$$\begin{aligned} \ell_C(\Theta) \propto \sum_{\mathbf{E} \in \mathcal{E}} \sum_{(\mathbf{h}, \tau) \in \Lambda_{\mathcal{S}} \times \Lambda_{\mathcal{T}}} \sum_{(\mathbf{s}, t) \in \mathcal{N}_{\mathbf{E}}(\mathbf{h}, \tau)} k_{\mathbf{E}}(\mathbf{s}, t) \log \chi_r(\mathbf{h}, \tau; \Theta, \mathbf{V}_{\mathbf{E}}) \\ + (1 - k_{\mathbf{E}}(\mathbf{s}, t)) \log(1 - \chi_r(\mathbf{h}, \tau; \Theta, \mathbf{V}_{\mathbf{E}})). \end{aligned} \quad (2)$$

The final inference step consists in maximizing the composite log-likelihood  $\ell_C(\Theta)$  with respect to the variogram parameters  $\Theta$ .

#### 4.4 Advection and parametric transformation

Advection velocities may be either known and directly specified in the model, or estimated from the data when unavailable. In our case, episode-specific empirical velocity vectors are inferred from rainfall barycenter displacements (see [Section 5](#)), and their estimation uncertainty is handled with a parametric transformation acting on their magnitude. For each episode an empirical velocity vector  $\mathbf{V}^{\text{emp}}$  is estimated from the data. This empirical velocity vector is not used directly in the model, but is mapped to an effective velocity vector with the transformation  $\mathcal{A}(\cdot)$ . The transformation acts only on the magnitude of the velocity vector, while preserving its direction. For any non-zero empirical velocity vector  $\mathbf{V}^{\text{emp}}$ ,

$$\mathcal{A}(\mathbf{V}^{\text{emp}}) = \eta_1 \|\mathbf{V}^{\text{emp}}\|^{\eta_2} \frac{\mathbf{V}^{\text{emp}}}{\|\mathbf{V}^{\text{emp}}\|}.$$

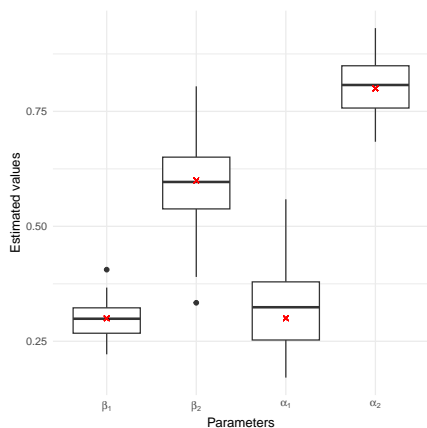
The advection associated with episode  $\mathbf{E} \in \mathcal{E}$  is given by  $\mathbf{V}_{\mathbf{E}} = \mathcal{A}(\mathbf{V}_{\mathbf{E}}^{\text{emp}})$ . The apparent episode-specific advection  $\mathbf{V}_{\mathbf{E}}$  is therefore fully determined by the parameters  $\eta_1$  and  $\eta_2$ . The new extended parameter vector becomes  $\tilde{\Theta} = (\beta_1, \beta_2, \alpha_1, \alpha_2, \eta_1, \eta_2)$  for all episodes and is estimated by maximizing the composite log-likelihood  $\ell_C(\tilde{\Theta})$  given in ((2)) for a specific episode  $\mathbf{E}$ , expressed as  $\chi_r(\mathbf{h}, \tau; \tilde{\Theta}, \mathbf{V}_{\mathbf{E}}^{\text{emp}})$ .

#### 4.5 Validation on simulated $r$ -Pareto processes

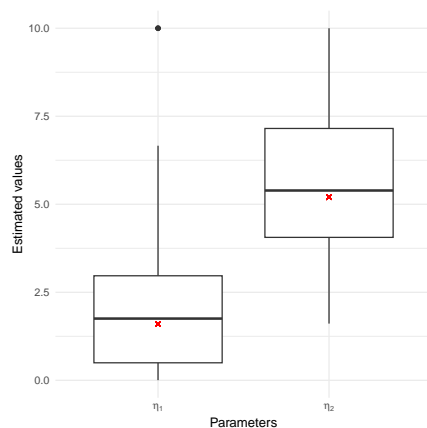
The proposed inference methodology is validated using simulated  $r$ -Pareto processes with known parameters. The simulation of  $r$ -Pareto processes is based on the spectral representation of spatio-temporal Brown-Resnick processes. Specifically, we adapt the simulation algorithm proposed by [Leber 2015](#), which itself relies on exact simulation techniques for spatial max-stable

processes developed in [Dombry et al. 2016](#). The  $r$ -Pareto processes are simulated on a regular grid of  $n$  spatial locations over a period of  $\delta$  time steps. A threshold  $u = 1$  is used to define the  $r$ -exceedances, and the risk function is chosen as  $r(\mathbf{X}) = X_{\mathbf{s}_0, t_0}$ , where  $\mathbf{s}_0$  is randomly selected among the spatial locations and  $t_0 = 0$  corresponds to the first time step of each simulated episode. Different sets of simulations are generated using known variogram parameters  $\tilde{\Theta}$ .

Three simulation settings are considered to assess the performance of the proposed inference methodology under different advection configurations. For each setting, 50 independent simulations of  $r$ -Pareto processes are generated, each consisting of 500 replicates of  $n = 49$  spatial locations over  $\delta = 24$  or 12 time steps. [Figure 3](#) illustrates the results obtained when the advection varies across episodes and the parameters  $(\eta_1, \eta_2)$  are jointly estimated together with the variogram parameters. Despite the higher number of parameters,  $(\beta_1, \beta_2, \alpha_1, \alpha_2)$  remain well identified. As expected, higher variability is mainly observed for the advection parameters  $(\eta_1, \eta_2)$ , which remain reasonably well estimated but with a compensatory effect between them, *i.e.* different combination can lead to similar velocity vectors. [Figure 4](#) depicts the estimation results obtained when the advection parameters  $(\eta_1, \eta_2)$  are fixed to their true values. In this case, the estimation results are comparable to those obtained when  $(\eta_1, \eta_2)$  are estimated, with accurate recovery of the variogram parameters. However, fixing the advection parameters can reduce the variability of the estimates, especially when dealing with real data where the advection estimation may be more uncertain.



(a)  $\beta_1 = 0.3, \beta_2 = 0.6, \alpha_1 = 0.3, \alpha_2 = 0.8$



(b)  $\eta_1 = 1.6, \eta_2 = 5.2$

Figure 3: Estimations of variogram parameters with maximum likelihood optimization on  $r$ -Pareto simulations with 49 sites and 24 time observations. The true parameters are indicated by red crosses. Here random advection by replicate (episode) is considered.

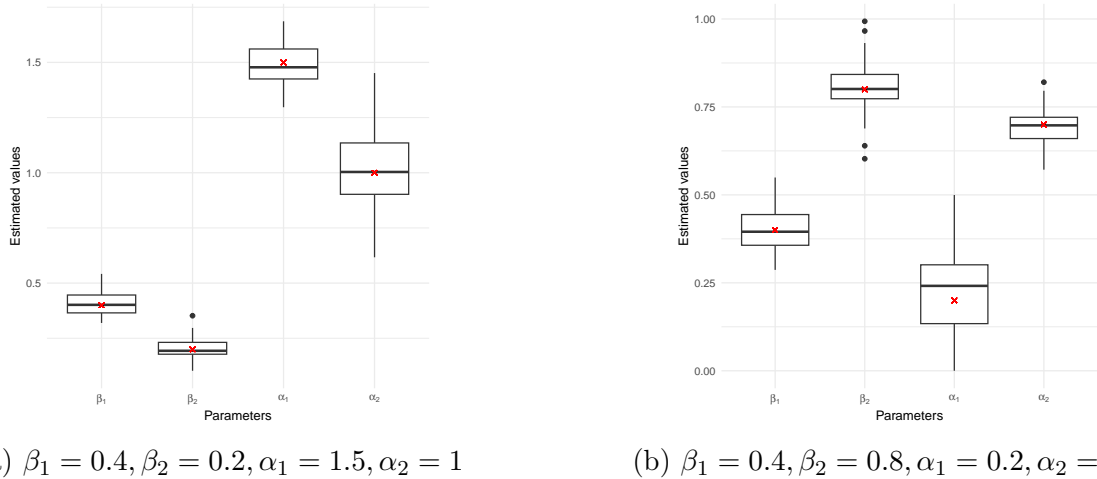


Figure 4: Estimations of variogram parameters with maximum likelihood optimization on  $r$ -Pareto simulations with 49 sites and 12 time observations. The true parameters are indicated by red crosses. We use a random advection by replicate (episode) with fixed  $\eta_1 = 0.5$  and  $\eta_2 = 1.6$ .

## 5. Application to rainfall data

In this section, the proposed spatio-temporal stochastic precipitation generator is applied to rainfall data from the OMSEV network in Montpellier. The marginal distributions are estimated, and the use of a common distribution is justified. The dependence structure of extremes is investigated by evaluating the adequacy of the non-separable variogram model, describing the selection of extreme episodes, and the advection estimation procedure is explained. This is followed by the inference of the spatio-temporal extremal dependence structure using both COMEPHORE and OMSEV datasets. Finally, the performance of the stochastic precipitation generator is assessed by comparing the simulated and observed rainfall fields at OMSEV sites, with a particular focus on the representation of extreme rainfall events. A final stochastic precipitation generator is constructed on a regular grid covering the entire area of interest.

### 5.1 Estimation of marginal distributions (OMSEV)

The EGPD model is fitted to rainfall data from the OMSEV network in order to assess its ability to represent the marginal distribution of positive rainfall intensities at each site. To account for the discretization induced by the finite measurement precision of the rain gauges, a small left-censoring is introduced, chosen according to a local goodness-of-fit criterion based on the Root Mean Square Error (RMSE), following [Haruna et al. 2023](#). Possible censoring thresholds are restricted to multiples of the gauge precision,  $p \approx 0.2153$  mm, *i.e.* values of the form  $k \times p$  with  $k \in \mathbb{N}$ . The final censoring threshold is set to  $p$  for most sites, and to  $2p$  for three sites (CEFE, Archie, and CNRS). The quantile-quantile plots displayed in [Figure 5](#) illustrate an overall good agreement between the fitted EGPD and the empirical rainfall distributions for four sites of the OMSEV network. The same level of agreement is observed at all other sites (not shown). No systematic deviations are observed in the upper tail, suggesting that

the extreme rainfall behavior is well captured by the EGD model. The distribution of the estimated EGD parameters across the OMSEV network is summarized in Figure 6. The shape parameter  $\xi$  is positive at all sites, with values ranging approximately between 0.25 and 0.30, indicating heavy-tailed rainfall intensity distributions. Estimated scale parameters  $\sigma$  mostly lie between 0.60 and 0.75, reflecting moderate variability in rainfall intensities across sites. It is consistent with short-duration rainfall data, which typically exhibit lower variability compared to longer-duration accumulations. Finally, the lower-tail parameters  $\kappa$  generally fall between 0.20 and 0.25, indicating heavier mass near small rainfall intensities relatively to the central part of the distribution. This is consistent with the short-duration nature of the data that leads to a larger proportion of small rainfall values compared to longer-duration accumulations. The largest  $\kappa$  outlier corresponds to the Archie site. This site is different from the others because of an interruption of measurements in 2023, which can explain differences in parameter estimates. Overall, these results seem to indicate that the EGD provides a relevant representation of the marginal rainfall distributions at all sites in the network.

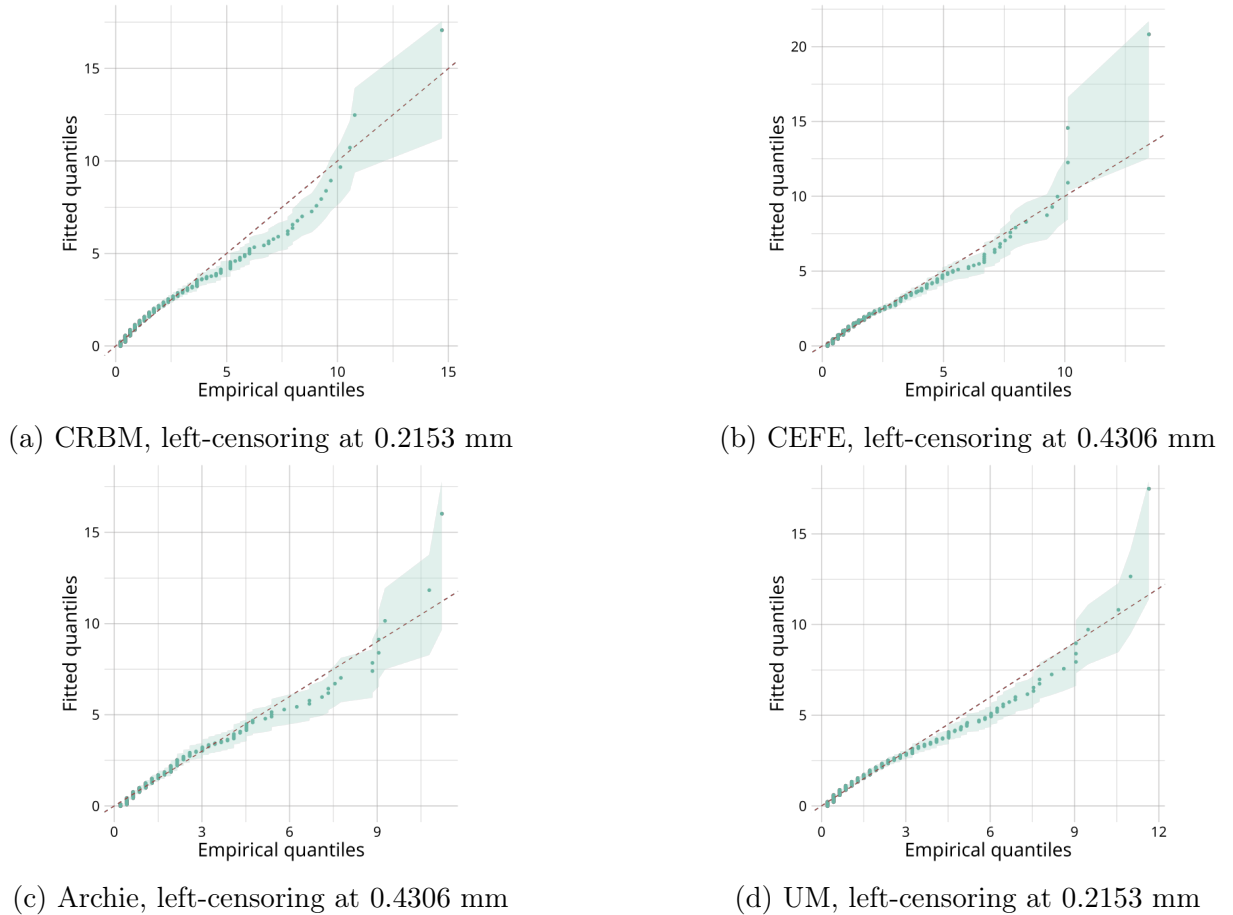


Figure 5: Quantile-quantile plot of the EGD fitting with bootstrap confidence intervals on four rain gauges of the OMSEV network with site-specific left-censoring.

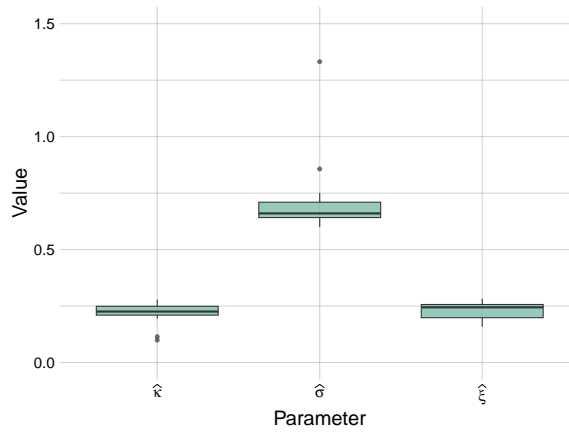


Figure 6: Boxplot of EGD parameter estimates across the OMSEV network with site-specific left-censoring.

The use of common EGD parameters across all sites is motivated by the absence of clear evidence of spatial heterogeneity in extreme rainfall marginals. Based on these complementary diagnostics, a common marginal model is assumed for the OMSEV network. Global Moran’s  $I$  test is applied to the estimated EGD parameters to detect possible spatial autocorrelation. For all parameters, the associated  $p$ -values are large, indicating that the null hypothesis of no global spatial autocorrelation cannot be rejected for each parameter (see Table 1). The spatial homogeneity of extreme rainfall is examined by comparing the distributions of exceedances between sites using the pairwise Anderson–Darling test. The results indicate that, for a large majority of site pairs, the null hypothesis of identical upper-tail distributions cannot be rejected based on the Anderson–Darling test. Specifically, for approximately 76% of the 136 pairwise comparisons, no significant difference is detected in the tail behavior above the  $q = 0.90$  quantile. Taken together, these results suggest that the marginal distributions of extreme rainfall are assumed to be approximately identical across the OMSEV network.

Table 1: Moran’s  $I$  test for global spatial autocorrelation in EGD parameters. The test is performed using the 4 nearest neighbors for each site. Reported  $p$ -values correspond to two-sided tests assessing the null hypothesis of no global spatial autocorrelation.

Parameter	Moran’s $I$	$p$ -value
$\xi$	−0.211	0.252
$\sigma$	−0.002	0.446
$\kappa$	−0.098	0.765

The marginal common parameters for the OMSEV network are estimated by fitting an EGD across all sites together, with left censoring at the gauge precision  $p$ , and by jointly estimating the probability of zero rainfall. The final parameter estimates are reported in Table 2. These will be used as common marginal parameters for the final stochastic precipitation generator and for the transformation of simulated values from the Pareto scale to the rainfall scale (see Section 3).

Table 2: Estimated common marginal parameters for the OMSEV network.

Parameter	$\hat{p}_0$	$\hat{\xi}$	$\hat{\sigma}$	$\hat{\kappa}$
Estimate	0.989	0.262	0.591	0.270

## 5.2 Empirical evidence of space-time non-separability

We investigate the space-time structure of extremal dependence using empirical spatio-temporal extremal variogram estimated from the extremogram in Equation ((1)). Under a separable space-time structure, the spatial variogram curves are expected to be proportional across temporal lags. Figure 7 shows that the empirical variogram exhibits clear changes in curves shape across different temporal lags, indicating an interaction between spatial and temporal dependence. This behavior provides strong empirical evidence against a separable spatio-temporal variogram for extreme rainfall in the OMSEV data. This justifies the non-separable variogram introduced in our model.

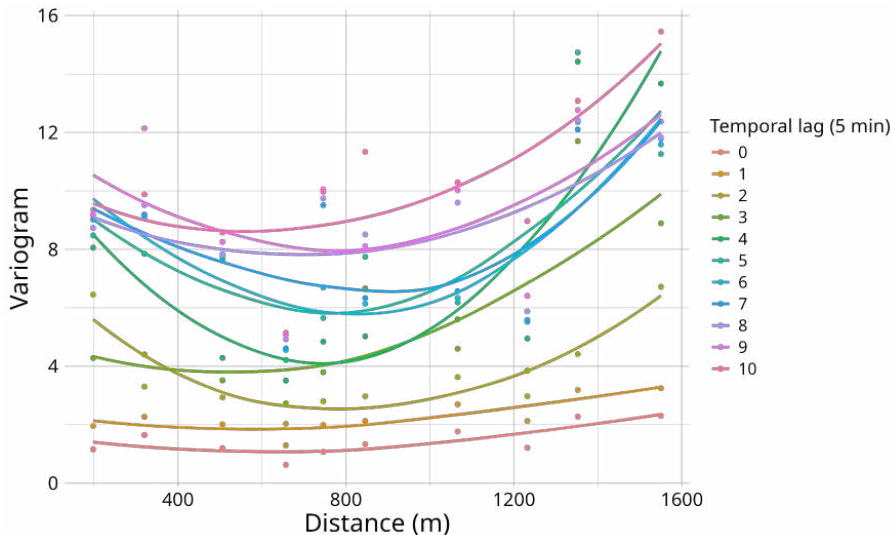


Figure 7: Empirical spatio-temporal variogram of the extreme OMSEV data for different temporal lags (in 5 minutes) over the spatial distance (in meters) and quantile  $q = 0.95$ .

## 5.3 Episode configuration

Extreme episodes are identified by selecting conditioning points exceeding a spatio-temporal quantile  $q$ , a duration  $\delta$  and a minimum spatial separation  $d_{\min}$  between episode. It aims to ensure weak dependence between selected episodes while retaining a sufficient number of episodes for inference.

To select an appropriate quantile threshold  $q$  for defining extreme episodes in the OMSEV data, we examine the number of joint exceedances observed at various spatial distances and temporal lags. For this purpose, we compute the number of joint exceedances above different quantiles  $q$  and we keep the quantile  $q = 0.95$  as a compromise between the representation of

extremes and sample size requirements. It allows a minimum of 40 spatial joint exceedances per spatial lag and a minimum of 20 temporal joint exceedances per temporal lag (see [Appendix A](#)).

An episode duration of  $\delta = 1$  hour (*i.e.*, 12 time steps of 5 minutes) is selected for the OMSEV data. We try several possibilities and the choice of  $\delta = 1$  hour represents a reasonable compromise between temporal interpretability, approximate independence between episodes, and a sufficient sample size for inference. This duration is consistent with the temporal resolution of the COMEPHORE data used for the advection estimation. A similar approach is performed to determine the minimum spatial separation  $d_{\min}$  between episodes. A value of  $d_{\min} = 1200$  meters is chosen to balance independence and sample size for inference (see [Appendix A](#)).

Regarding the COMEPHORE data, a similar analyses is employed to determine the episode configuration parameters. The same quantile threshold  $q = 0.95$  is adopted to define extreme episodes to ensure consistency with the OMSEV data analysis. Given the hourly time resolution of the COMEPHORE data, episodes are defined over  $\delta = 24$  hours periods, starting from a conditioning exceedance, corresponding to a daily episode duration. The minimum spatial separation between episodes is set to  $d_{\min} = 5$  km preserving a sufficient number of episodes for inference and ensuring approximate independence between episodes.

A summary of the episode configuration parameters adopted for both the OMSEV and COMEPHORE datasets is provided in [Table 3](#). Under such configurations, a total of 384 extreme episodes are considered in the OMSEV dataset and 1130 in the COMEPHORE dataset.

Table 3: Summary of the episode configuration parameters adopted for the OMSEV and COMEPHORE datasets and the resulting number of selected episodes.

Datset	OMSEV	COMEPHORE
Quantile $q$	0.95	0.95
Episode duration $\delta$	60 minutes	24 hours
Minimum spatial separation $d_{\min}$	1200 m	5 km
Number of selected episodes $ \mathcal{E} $	384	1130

## 5.4 Estimation of advection

For each extreme rainfall episode from the OMSEV dataset, a velocity vector is required to characterize the propagation of rainfall storm. Due to the irregular spatial distribution of rain gauges and the limited spatial extent of the OMSEV network, such a vector cannot in general be reliably estimated from OMSEV data alone. To overcome this limitation, we rely on the COMEPHORE dataset which covers a much larger spatial domain and provides rainfall estimates at higher spatial and temporal resolution. COMEPHORE therefore offers a more comprehensive view of the displacement of rainfall systems.

The duration of OMSEV extreme episodes is one hour, which matches the time resolution of COMEPHORE data. Therefore, for each OMSEV episode, the corresponding hourly COMEPHORE time is identified and used to estimate the advection term. The empirical velo-

city vector  $\mathbf{V}_{\text{COM}}^{\text{emp}}$  is assigned based on COMEPHORE episodes occurring over a specific time window extending two hours before and after the OMSEV episode. Advection is estimated by tracking the displacement of rainfall intensity patterns over time. At each timestamp, the rainfall field is summarized by its barycenter, defined as the center of mass of the rainfall field, where rainfall intensities act as weights. The temporal evolution of these barycenters provides successive displacement vectors. By averaging these vectors over time, we obtain an empirical advection vector for the episode. An illustrative example of this procedure is shown in Figure 8.

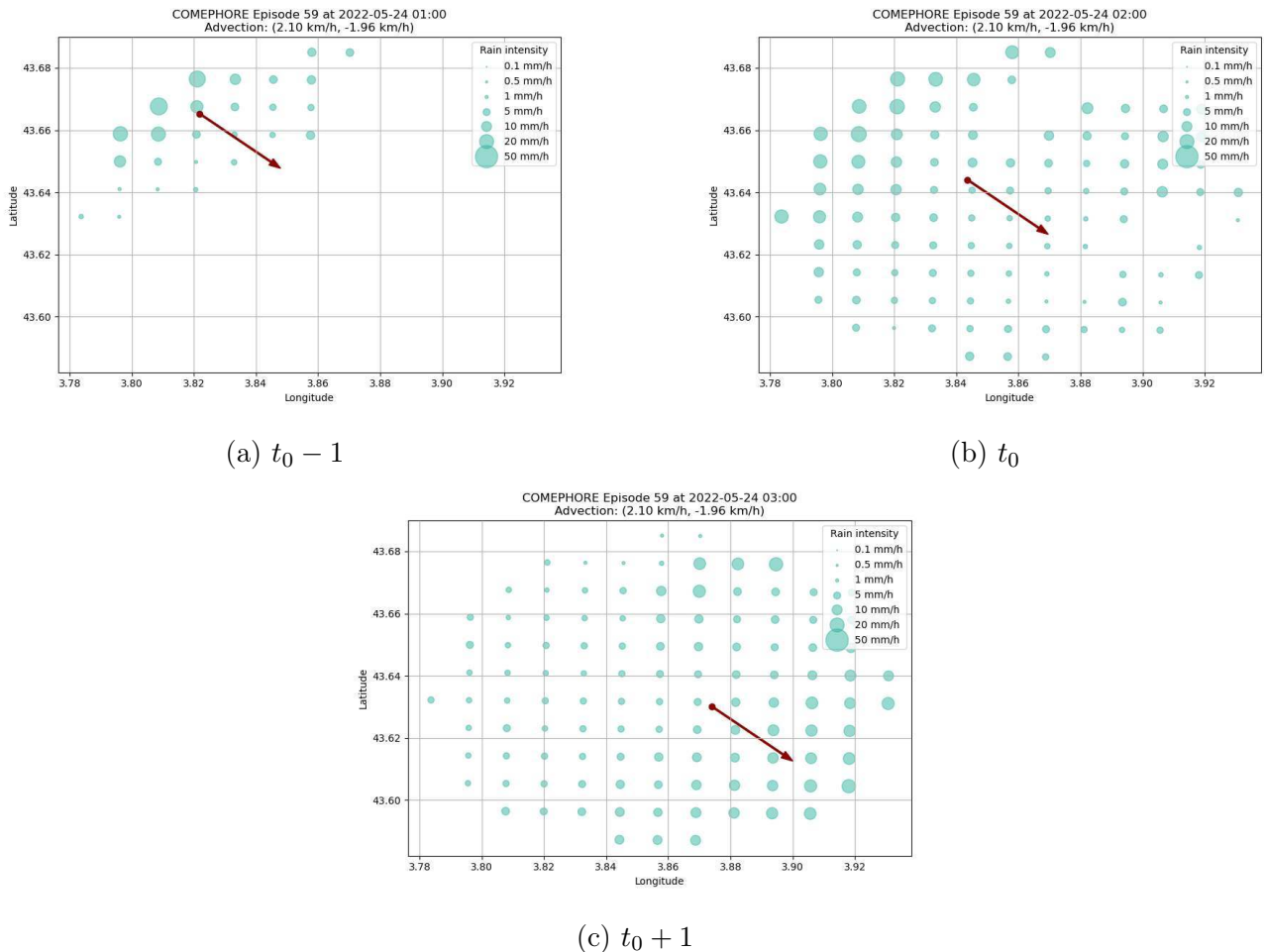


Figure 8: Extreme rainfall episode from COMEPHORE on May 24, 2022. Rainfall intensity is represented by point size. The empirical velocity vector (red arrow), estimated over the episode, is shown at the barycenter position at each time step. Only the barycenter location changes between panels. Estimated advection:  $(2.10, -1.96)$  km/h.

Due to differences in spatial coverage and event detection, some OMSEV episodes do not correspond to any COMEPHORE episode. In such cases, the advection is estimated directly from the OMSEV network, yielding an empirical vector  $\mathbf{V}_{\text{OMSEV}}^{\text{emp}}$ . Although this estimate is much less precise because of the limited spatial extent of OMSEV network, it still provides partial information on the local displacement of precipitation and constitutes the only available

option. The final velocity vector  $\mathbf{V}^{\text{final}}$  is defined as

$$\mathbf{V}^{\text{final}} = \begin{cases} \mathcal{A}(\mathbf{V}_{\text{COM}}^{\text{emp}}), & \text{if a corresponding COMEPHORE episode exists,} \\ \mathcal{A}(\mathbf{V}_{\text{OMSEV}}^{\text{emp}}), & \text{otherwise.} \end{cases}$$

The function  $\mathcal{A}(\cdot)$  denotes the transformation described in [Section 4.4](#).

## 5.5 Variogram estimation

The OMSEV variogram is estimated using a strategy based on COMEPHORE data. Variogram parameters, including the advection transformation parameters  $\eta_1$  and  $\eta_2$ , are estimated from COMEPHORE episodes using the composite likelihood described in [Section 4.3](#). Empirical velocity vectors are computed as detailed in [Section 5.4](#), and weighted least-squares estimates following [Buhl et al. 2019](#) are used to initialize the optimization. These estimates are then used both to initialize the OMSEV variogram optimization and to fix the advection parameters.

Preliminary analyses reveal that the range of the advection speeds has a non-negligible impact on the estimated variogram parameters. To ensure comparability between both datasets empirical advection terms (before transformation), we perform the COMEPHORE optimization on a restricted range of advection speeds matching those observed over OMSEV data, *i.e.*  $\|\mathbf{V}\| \leq 5.6$  km/h. This restriction removes around 3% of the episodes and we keep a total of 1097 episodes for the COMEPHORE estimation.

The resulting COMEPHORE parameter estimates are reported in [Table 4](#). We observe that the temporal component  $\hat{\beta}_2$  is larger than the spatial one  $\hat{\beta}_1$ , indicating that temporal variability dominates. The small values of  $\hat{\alpha}_1$  and  $\hat{\alpha}_2$  suggest a high degree of irregularity in the spatial and temporal dependence structure of extremes. This is consistent with convective extreme rainfall, especially given the small spatial exponent  $\hat{\alpha}_1$ . The estimated advection parameters  $\hat{\eta}_1 = 1.621$  and  $\hat{\eta}_2 = 5.219$  indicate a strong non-linear transformation of the empirical velocity vectors. In particular, the large value of  $\hat{\eta}_2$  can lead to unrealistically high transformed advection speeds, although this affects only a small number of episodes. Indeed, there are 43 episodes (approximately 4% of COMEPHORE episodes) for which the transformed advection speed exceeds 150 km/h, and 13 for which it exceeds 1000 km/h, corresponding to outliers. We use 150 km/h as an upper bound for the transformed advection speed in the subsequent analysis. This restriction does not remove much episodes from the OMSEV dataset after transformation on their corresponding advection speeds. Only 9 episodes are removed (approximately 2%) before the variogram parameter estimation. The COMEPHORE parameter estimates are used as initial values for the OMSEV optimization, with the advection parameters  $\eta_1$  and  $\eta_2$  fixed. The resulting OMSEV parameter estimates, with month-leave-one-out Jackknife confidence intervals, are presented in [Table 5](#). As for COMEPHORE, the temporal component remains larger than the spatial one and the estimated smoothness parameters  $\alpha_1$  and  $\alpha_2$  indicate strong irregularity.

The adequacy of the fitted model is assessed by comparing empirical and fitted  $r$ -extremograms

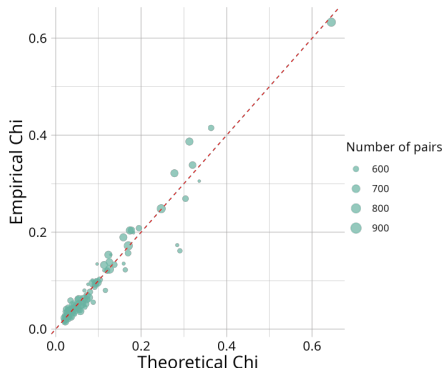
for both datasets in Figure 9. In both cases, the fitted  $r$ -extremograms closely match the empirical ones across a range of spatial and temporal lags, indicating that the proposed model effectively captures the extremal dependence structure of both COMEPHORE and OMSEV data.

Table 4: COMEPHORE results for OMSEV-like advection class ( $\|\mathbf{V}\| \in [0, 5.6]$  km/h) with  $|\mathcal{E}| = 1097$ .

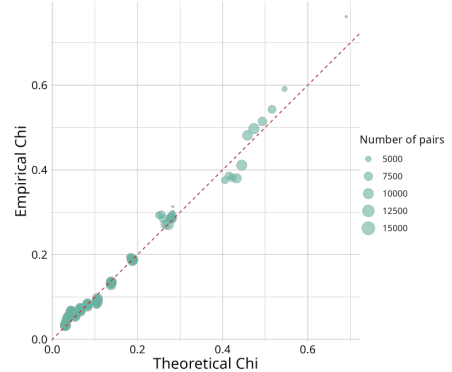
$\hat{\beta}_1$	$\hat{\beta}_2$	$\hat{\alpha}_1$	$\hat{\alpha}_2$	$\hat{\eta}_1$	$\hat{\eta}_2$
0.308	0.602	0.342	0.761	1.621	5.219

Table 5: Parameter estimates for OMSEV advection classes with month-leave-one-out Jackknife confidence intervals. Parameters  $\eta_1$  and  $\eta_2$  are fixed to the COMEPHORE estimates. Number of episodes:  $|\mathcal{E}| = 375$ .

	km/h	m/5 min
$\hat{\beta}_1$	1.090 [0.780, 1.401]	0.230 [0.087, 0.560]
$\hat{\beta}_2$	4.628 [3.383, 5.873]	0.786 [0.324, 1.767]
$\hat{\alpha}_1$	0.225 [0.133, 0.317]	0.225 [0.133, 0.317]
$\hat{\alpha}_2$	0.713 [0.483, 0.944]	0.713 [0.483, 0.944]



(a) OMSEV data



(b) COMEPHORE data

Figure 9: Empirical against theoretical  $r$ -extremogram for each spatio-temporal lags with estimated parameters according to pairs number within the same spatio-temporal lag.

## 6. Stochastic rainfall generation

This section presents the final stochastic rainfall generator obtained by combining the marginal and dependence models developed in the previous sections and evaluates its ability to reproduce the marginal and dependence structure of extreme rainfall episodes observed in the OMSEV dataset.

## 6.1 Validation of simulated rainfall episodes at OMSEV sites

Rainfall simulations are performed by generating episodes of the  $r$ -Pareto process given the occurrence of an extreme event at a conditioning location within the OMSEV rain gauge network. For each observed episode, we simulate a new episode by conditioning on the same site using the same threshold and the same empirical velocity vector, which will be transformed using the estimated parameters  $\hat{\eta}_1$  and  $\hat{\eta}_2$ . The simulated  $r$ -Pareto processes are then transformed back to the original rainfall scale as described in [Section 3.4](#). For the validation we consider the marginal distributions fitted at each site separately and for the final simulations we use the common marginal distribution fitted across all sites, as justified in [Section 5.1](#).

To validate the marginal behavior and dependence behavior of rainfall intensities, we consider the 384 extreme episodes identified in the OMSEV dataset (see [Section 5.3](#)) and we generate 100 conditional simulations for each episode. We compare the distribution of strictly positive rainfall values at each site observed during extreme episodes with those produced by the simulations.

[Figure 10](#) compares the densities of strictly positive rainfall values between observations and simulations for two sites of the OMSEV network. Without correction (top row), simulated distributions agree well with observations at moderate and high intensities but underestimate the frequency of low rainfall values (below 1.5 mm). This difference is mainly due to the discretization of observed rainfall, whereas simulations are continuous by construction, making comparisons at low values unreliable. To account for this effect, a discretization correction is applied to simulations: values strictly between 0 and the gauge precision  $p$  are mapped to  $p$ , while larger values remain unchanged. As shown in the bottom row, this adjustment substantially improves the agreement at low intensities while preserving the upper-tail behavior. Overall, the simulated marginal distributions are consistent with observations across the network (not shown), although simulations exhibit slightly more high-intensity values, likely due to the absence of an upper bound and the presence of occasional extreme simulated outliers. These results indicate that the proposed model adequately reproduces the marginal distribution of rainfall intensities during extreme episodes.

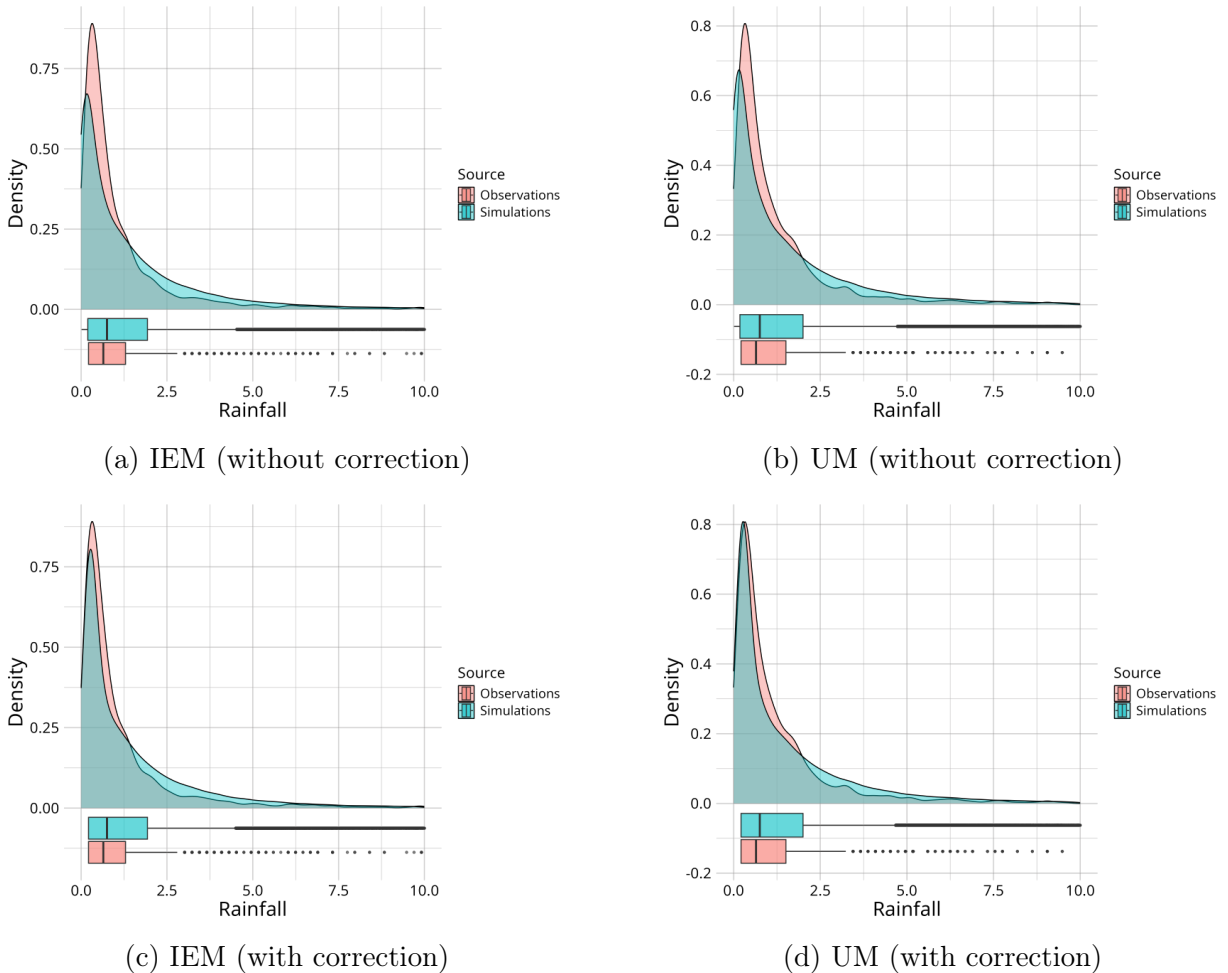


Figure 10: Density of strictly positive rainfall values for observed against simulated episodes for two selected sites of the OMSEV network. Top row: without correction for the discretization effect. Bottom row: with a correction on low simulated values to account for discretization in observations. For better visibility, only values below 10 mm are shown.

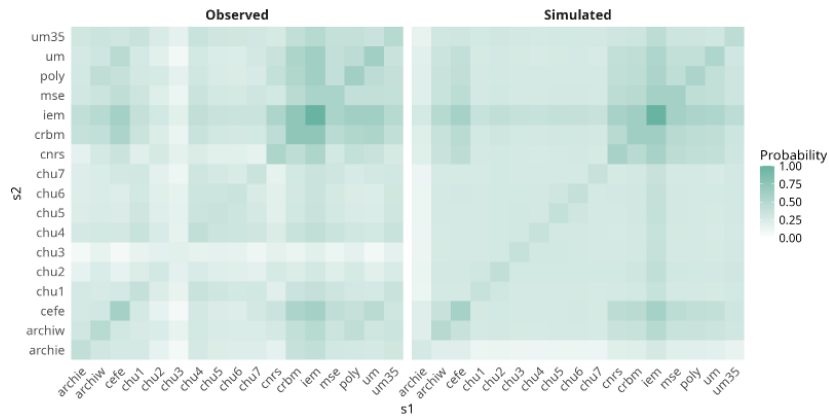
To evaluate the ability of the model to capture the dependence structure of rainfall extremes, we compute the conditional trivariate exceedance probabilities

$$\mathbb{P}(X_{\mathbf{s}_1} > u, X_{\mathbf{s}_2} > u | X_{\mathbf{s}} > u)$$

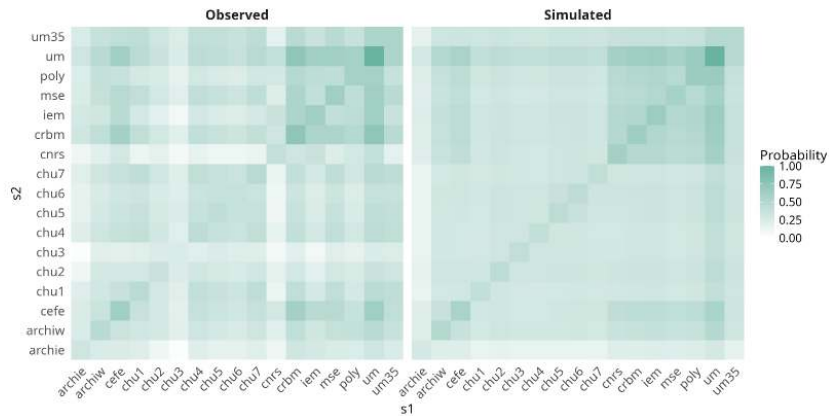
for any pairs of sites  $(\mathbf{s}_1, \mathbf{s}_2) \in \mathcal{S}^2$ , given an exceedance at a conditioning site  $\mathbf{s} \in \mathcal{S}$ . The threshold  $u$  is chosen as the empirical 95% quantile of the data. These probabilities are estimated empirically from both observed and simulated data by counting joint exceedances at the three sites  $(\mathbf{s}_1, \mathbf{s}_2, \mathbf{s})$  and dividing by the number of exceedances at the conditioning site  $\mathbf{s}$ . The results are shown in Figure 11 for two selected conditioning sites. We observe that the largest conditional probabilities are generally well reproduced by the simulations, whereas smaller probabilities tend to be less accurately captured.

As a complementary summary indicator of the dependence structure, we consider the distribution of cumulative rainfall within episodes. This quantity reflects both the number of exceedances occurring across the network and their associated intensities. Cumulative rainfall is defined as the sum of rainfall intensities over all sites and time steps within an episode,

providing a global measure of event intensity. The observed and simulated distributions are compared in Figure 12. The simulated distribution exhibit a slightly larger proportion of low cumulative rainfall values with a lower median than observed data while the bulk of the distribution and the upper tail is well captured. This behavior is expected from the conditional simulation framework: each episode is generated conditionally on an exceedance at a single conditioning site, so that some simulated realizations have a single exceedance while rainfall at other sites remains close to zero. In contrast, observed episodes more frequently involve multiple exceedances during the episode across the network, which leads to larger cumulative totals even for moderate events. Consequently, the simulated cumulative distribution tends to underestimate the lower range of cumulative rainfall values.



$$(a) \mathbb{P}(X_{s_1} > u, X_{s_2} > u | X_{IEM} > u)$$



$$(b) \mathbb{P}(X_{s_1} > u, X_{s_2} > u | X_{UM} > u)$$

Figure 11: Conditional trivariate exceedance probabilities according to an excess at one site from observations versus simulations.

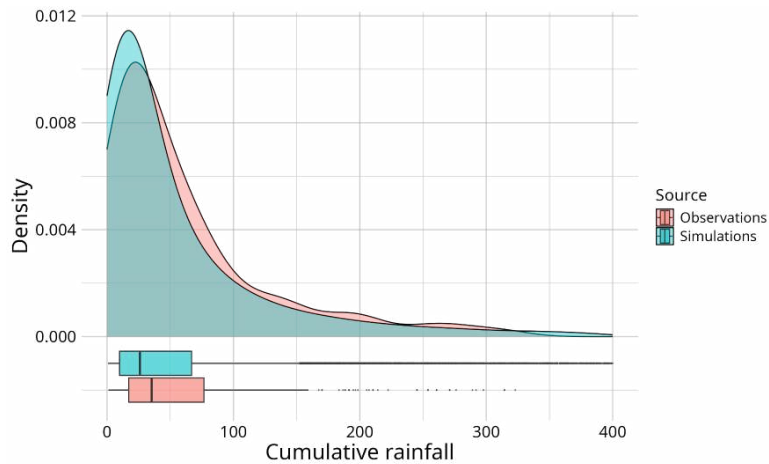


Figure 12: Density of cumulative rainfall over all sites within episodes for observed and simulated data. For better visibility, only values below 400 mm are shown.

The proposed model is able to reproduce both the marginal distribution of rainfall intensities during extreme episodes and the main features of the extremal dependence structure. The agreement is better for larger probabilities and higher rainfall accumulations. This is consistent with the primary objective of the model, which is to capture the behavior of extremes and their extremal dependence.

## 6.2 Final simulations on a regular grid

We now use the fitted model to simulate rainfall fields on a regular grid covering the OMSEV domain at fine spatial resolution. Simulations are performed on a regular grid with 100 m pixels, assuming spatially stationary marginal distributions with parameters given in [Table 2](#), and using the fitted dependence model described in [Table 5](#). An example of a simulated extreme rainfall episode is shown in [Figure 13](#). In this example, the conditional exceedance is imposed at a randomly selected grid pixel, and a randomly sampled velocity vector is applied. The resulting rainfall field exhibits a coherent displacement over time, consistent with the given advection direction. These simulations demonstrate the ability of the framework to generate continuous extreme rainfall episode scenarios on a regular grid at fine resolution. The continuous nature of the simulations allows for more realistic rainfall patterns that cannot be directly captured from the discrete rain gauge network alone.

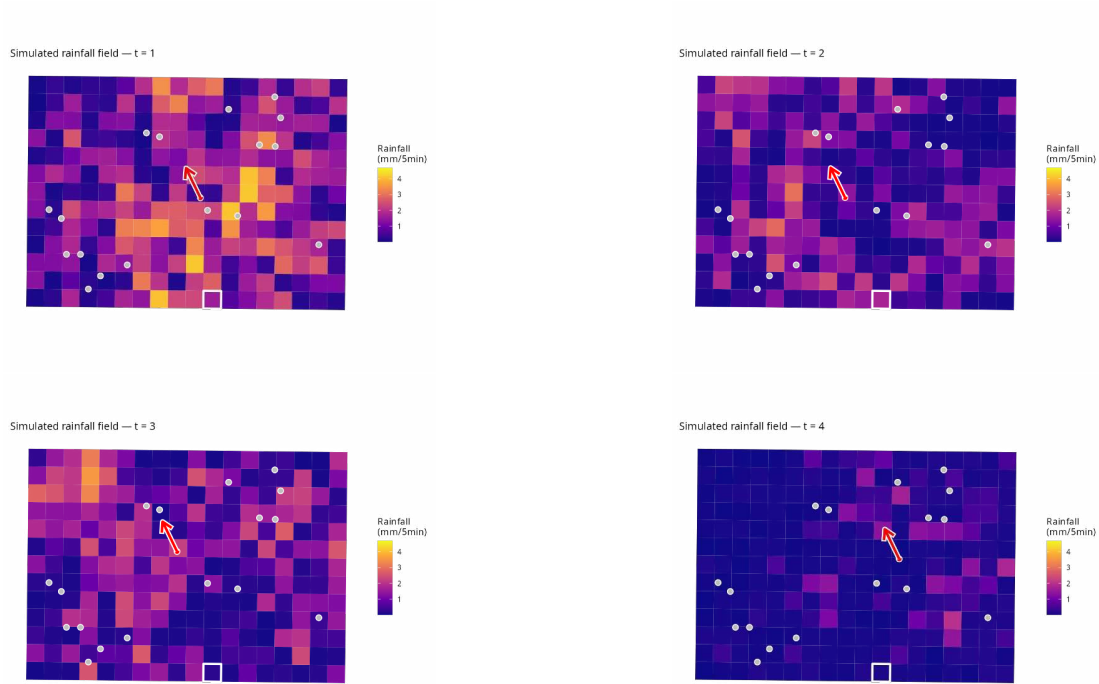


Figure 13: Simulated rainfall episode on a regular grid over the OMSEV area at the first four time steps. Rain gauge locations are shown as grey dots. The selected conditioning grid pixel is highlighted by a white square and the advection direction is indicated by a red arrow plotted at the barycenter of the rainfall field. Here  $\mathbf{V}_E = (-1, 2)$  km/h. A gif version is available [here](#).

## 7. Discussion and perspectives

In this work, we proposed a spatio-temporal stochastic framework for the simulation of extreme rainfall events at fine spatial and temporal scales that explicitly accounts for advection within the dependence structure. The approach combines flexible marginal modeling based on the EGPD with an advection-informed spatio-temporal variogram for the dependence structure. The framework was shown to accurately reproduce both the marginal behavior of extreme rainfall and its spatio-temporal dependence structure. The resulting stochastic rainfall generator can be applied on a regular grid at fine spatial resolution, making it suitable for applications such as risk assessment and hydrological impact studies. Although developed and validated on the OMSEV dataset, the methodology can be adapted to other high-resolution rainfall networks.

Despite its flexibility, the proposed modeling framework has some limitations at such a fine spatial and temporal scale and can be improved. A major source of uncertainty is the estimation of advection velocities. In this study, velocity vectors were mainly inferred from COMEPHORE data due to the limited spatial coverage and the irregularity of the OMSEV rain gauge network. Even with COMEPHORE data, the spatial extent of the study area (approximately 5 km around the OMSEV network) strongly constrains the range of detectable advection velocities. As a result, speeds above approximately 10 km/h cannot be identified and may be interpreted as null advection. In addition, differences in events detection between the

OMSEV and COMEPHORE datasets may lead to inconsistencies in the advection estimates, as extreme events detected by OMSEV data are not always captured by COMEPHORE data within the corresponding hour. A natural perspective would be to directly incorporate real wind data or advection information into the model. Such information would need to be available at sufficiently high spatial and temporal resolution to remain consistent with the rainfall data considered here.

Overall, the proposed framework provides a coherent and physically interpretable approach for the simulation of spatio-temporal extreme rainfall fields, and constitutes a promising basis for future developments and applications in this area.

## Code availability

The code used in this paper is available on the GitHub repository [chloesrcb/extreme-rainfall-generator](https://github.com/chloesrcb/extreme-rainfall-generator).

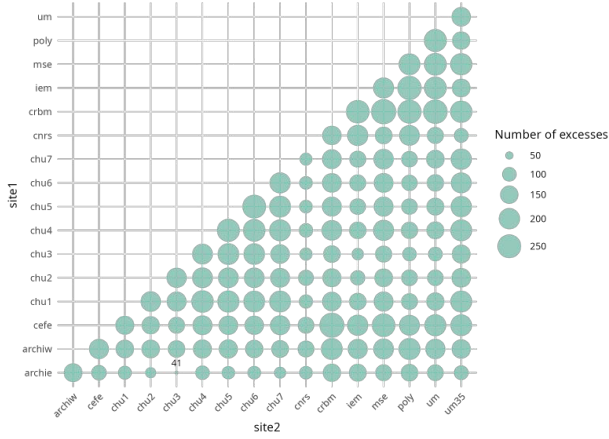
## References

- D. Allard, P. Ailliot, V. Monbet, and P. Naveau. *Stochastic weather generators: An overview of weather type models*, volume 156. 2015.
- L. Benoit and G. Mariethoz. Generating synthetic rainfall with geostatistical simulations. *Wiley Interdisciplinary Reviews: Water*, 4(2):e1199, 2017.
- L. Benoit, D. Allard, and G. Mariethoz. Stochastic Rainfall Modeling at Sub-kilometer Scale. 54(6):4108–4130, 2018. ISSN 1944-7973.
- P. Brunet, C. Bouvier, and L. Neppel. Retour d’expérience sur les crues des 6 et 7 octobre 2014 à Montpellier-Grabels (Hérault, France) : caractéristiques hydro-météorologiques et contexte historique de l’épisode. *Physio-Géo. Géographie physique et environnement*, 12:43–59, 2018. ISSN 1958-573X.
- S. Buhl, R. A. Davis, C. Klüppelberg, and C. Steinkohl. Semiparametric estimation for isotropic max-stable space-time processes. *Bernoulli*, 25:2508–2537, 2019.
- J. Carreau and Y. Bengio. A hybrid Pareto model for asymmetric fat-tailed data: the univariate case. *Extremes*, 12(1), 2009.
- N. L. Carrer and C. Gaetan. Distributional regression models for Extended Generalized Pareto distributions. *arXiv:2209.04660*, 2022.
- M. C. Casas, R. Rodríguez, and Á. Redaño. Analysis of extreme rainfall in Barcelona using a microscale rain gauge network. *Meteorological Applications: A journal of forecasting, practical applications, training techniques and modelling*, 17(1):117–123, 2010.

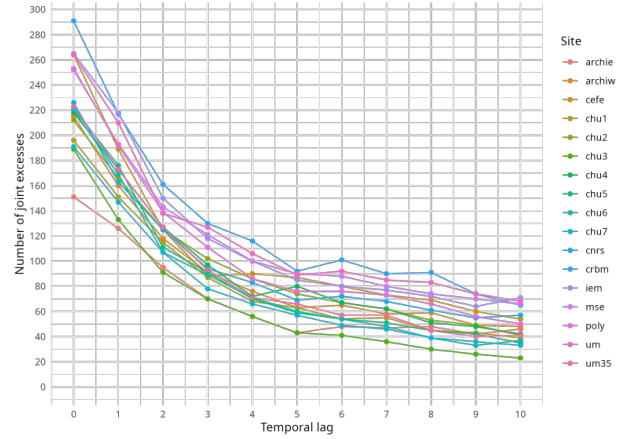
- S. Coles, J. Heffernan, and J. Tawn. Dependence measures for extreme value analyses. *Extremes*, 2:339–365, 1999.
- S. Coles, J. Bawa, L. Trenner, and P. Dorazio. *An introduction to statistical modeling of extreme values*, volume 208. Springer, 2001.
- A. C. Davison, S. A. Padoan, and M. Ribatet. Statistical modeling of spatial extremes. 2012.
- A. C. Davison, R. Huser, and E. Thibaud. Geostatistics of dependent and asymptotically independent extremes. *Mathematical Geosciences*, 45(5):511–529, 2013.
- R. De Fondeville and A. C. Davison. High-dimensional peaks-over-threshold inference. 105(3): 575–592, 2018. ISSN 0006-3444.
- C. Dombry, S. Engelke, and M. Oesting. Exact simulation of max-stable processes. 103(2): 303–317, 2016. ISSN 0006-3444, 1464-3510.
- C. Dombry, J. Legrand, and T. Opitz. Pareto processes for threshold exceedances in spatial extremes, 2024.
- A. Ferreira and L. De Haan. The generalized Pareto process; with a view towards application and simulation. 2014.
- P. Finaud-Guyot, V. Guinot, P. Marchand, L. Neppel, C. Salles, and G. Toulemonde. Rainfall data collected by the HSM urban observatory (OMSEV), 2023.
- C. Fouchier, J. Lavabre, P. Royet, and H. Felix. Inondations de septembre 2002 dans le Sud de la France - Analyse hydrologique et hydraulique au niveau des barrages écrêteurs du Vidourle. 2004.
- A. Haruna, J. Blanchet, and A.-C. Favre. Modeling intensity-duration-frequency curves for the whole range of non-zero precipitation: a comparison of models. *Water Resources Research*, 59(6):e2022WR033362, 2023.
- N. Hempelmann, C. Adeline, C. Pagé, and Y. Rodriguez-Dartois. Ville de Paris : Actualisation du diagnostic de vulnérabilités et de robustesses de Paris face aux changements climatiques et à la raréfaction des ressources - Cahier 2 : Les évolutions climatiques à Paris. *Ramboll*, 4, 2021.
- R. Huser and A. C. Davison. Space–time modelling of extreme events. *Journal of the Royal Statistical Society Series B: Statistical Methodology*, 76(2):439–461, 2014.
- D. Leber. Comparison of simulation methods of Brown–Resnick processes. Master’s thesis, Technische Universität München, Munich, Germany, 2015.
- E. Leblois and J.-D. Creutin. Space-time simulation of intermittent rainfall with prescribed advection field: Adaptation of the turning band method. 49(6):3375–3387, 2013. ISSN 1944-7973.

- P. Lucas-Picher, D. Argüeso, E. Brisson, Y. Trambly, P. Berg, A. Lemonsu, S. Kotlarski, and C. Caillaud. Convection-permitting modeling with regional climate models: Latest developments and next steps. *Wiley Interdisciplinary Reviews: Climate Change*, 12(6):e731, 2021.
- P. Naveau, R. Huser, P. Ribereau, and A. Hannart. Modeling jointly low, moderate, and heavy rainfall intensities without a threshold selection. *Water Resources Research*, 2016.
- F. Palacios-Rodríguez, G. Toulemonde, J. Carreau, and T. Opitz. Generalized Pareto processes for simulating space-time extreme events: an application to precipitation reanalyses. *Stochastic Environmental Research and Risk Assessment*, 34:2033–2052, 2020.
- I. Papastathopoulos and J. A. Tawn. Extended generalised Pareto models for tail estimation. 143(1):131–143, 2013. ISSN 0378-3758.
- R. Robin. Calibration du réseau de pluviographes de l’observatoire HSM « Eau dans la ville », 2021.
- C. Scarrott and A. MacDonald. A review of extreme value threshold estimation and uncertainty quantification. *REVSTAT-Statistical journal*, 10(1):33–60, 2012.
- M. Schleiss, S. Chamoun, and A. Berne. Stochastic simulation of intermittent rainfall using the concept of “dry drift”. 50(3):2329–2349, 2014. ISSN 1944-7973.
- P. Tabary, P. Dupuy, G. L’Henaff, C. Gueguen, L. Moulin, and O. Laurantin. A 10-year (1997—2006) reanalysis of Quantitative Precipitation Estimation over France: methodology and first results. *IAHS-AISH publication*, (351):255–260, 2012.
- D. S. Wilks and R. L. Wilby. The weather generation game: a review of stochastic weather models. *Progress in physical geography*, 23(3):329–357, 1999.

## A. Additional figures for episode configuration

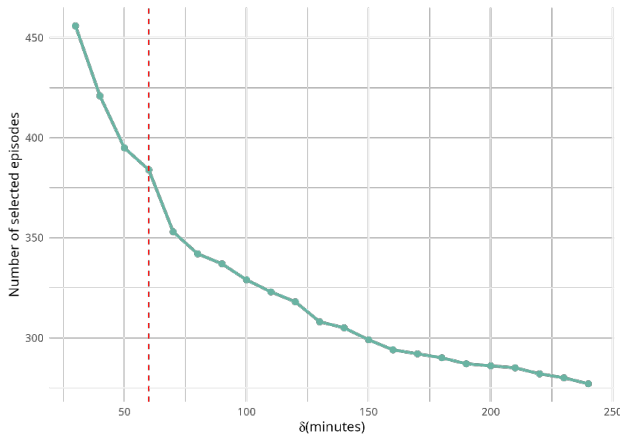


(a) Spatial joint exceedances

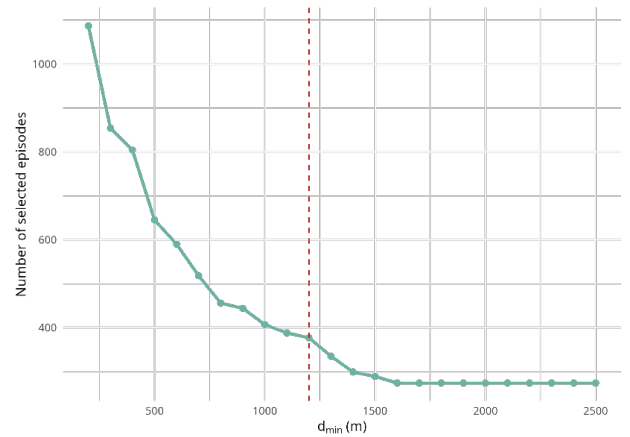


(b) Temporal joint exceedances

Figure 14: Number of joint exceedances according to spatial distance or temporal lag for the 0.95 quantile.



(a) By episode duration  $\delta$ .



(b) By minimum inter-episode distance  $d_{\min}$ .

Figure 15: Number of selected episodes according to episode configuration parameters on the OMSEV dataset for a quantile threshold  $q = 0.95$ . Figure (a) shows the effect of the minimum spatial separation  $d_{\min}$  on the number of selected episodes for a fixed episode duration  $\delta = 60$  minutes. Figure (b) shows the effect of the episode duration  $\delta$  on the number of selected episodes for a fixed spatial separation  $d_{\min} = 1200$  meters. In both figures, the final selected configuration corresponds to the red dashed vertical line.